Incorporating Spectral Similarity Into Markov Chain Geostatistical Cosimulation for Reducing Smoothing Effect in Land Cover Postclassification

Weixing Zhang, Weidong Li, Chuanrong Zhang, and Xiaojiang Li

***Abstract*—Spatial statistics provides useful methods for incorporating spatial dependence into land cover classification. However, the geometric features of land cover classes are difficult to be captured by geostatistical models due to smoothing effect. The objective of this study is to incorporate spectral similarity into the Markov chain random field (MCRF) cosimulation (coMCRF) model, that is, to propose a spectral similarity-enhanced MCRF cosimulation (SS-coMCRF) model, for land cover postclassification so that postclassification will cause less geometric loss. Two mutually complementary spectral similarity measures, Jaccard index and the spectral correlation measure, were employed as a constraining factor in SS-coMCRF. One medium spatial resolution scene with a complex landscape and one very high spatial resolution scene with an urban landscape were selected for case studies. Neural network classifier and support vector machine classifier were used to conduct land cover preclassifications. Both coMCRF and SS-coMCRF were used to postprocess preclassified images based on expert-interpreted sample datasets from multiple data sources. Compared with preclassified results that depend on only spectral information of pixels, postclassifications by both models achieved similar significant improvements in overall accuracy. However, compared with coMCRF, the SS-coMCRF model apparently improved postclassified land cover patterns by effectively capturing some geometric features (e.g., boundaries and linear stripes) and more details of land cover classes. In general, incorporating spectral similarity into land cover postclassification through SS-coMCRF may contribute significantly to the "shape" or geometric accuracy of classified land cover classes.**

***Index Terms*—Expert interpretation, geometric feature, land cover class, Markov chain random field, postclassification, preclassification, spectral similarity measure.**

I. Introduction

REMOTELY sensed images have been widely used in land cover classification because of their capability of detecting earth's surface spatially, temporally, and spectrally [1], [2]. However, it is still challenging to make a high-quality land cover map using remotely sensed images, especially in medium or coarse spatial resolutions, because of spectral confusion, complex landscapes, limitations of classification methods, and low quality of remotely sensed images [3], [4]. Despite these disadvantages, remotely sensed images still provide abundant information for land cover classification if an appropriate approach is used [5]. A large number of enhanced classification methods have been developed, such as artificial neural networks (NN) [6], [7], support vector machines (SVM) [8], [9], geostatistical classifier [10], [11], contextual classifiers [12], [13], knowledge-based algorithms [14], [15], Markov random field-based classifiers [16], and hybrid classifiers (e.g., a combination of pixel-based classifier and object-based classifier) [17]–[19].

Besides enhanced classification methods, postclassification operation is regarded as an effective way to improve the accuracy of a preclassified land cover map [20]. For example, Mesev [21] used population information in urban image postclassification sorting. To remove "speckled" or "salt and pepper" noise produced by pixel spectra-based classifiers, some noise removal methods were proposed [22]–[24]. In [25], postclassification correction was applied to improve land cover preclassification by incorporating ancillary data and knowledge-based logic rules. Textural analysis (using cooccurrence matrix) was used to conduct more accurate urban mapping from high spatial resolution satellite images [26], [27]. Stefanov *et al.* [28] and Kahya *et al.* [29] adopted an expert system to sort initial land cover classification results using ancillary data (such as land use data).

Tobler's first law of geography states that "Everything is related to everything else, but near things are more related than distant things" [30]. To a large extent, this implies that nearer pixels are more likely to belong to the same class. Therefore, spatial statistics may provide useful methods for incorporating spatial autocorrelation information into land cover classification. For example, in order to improve the classification of forest tree species, Carvalho *et al.* [31] used the direct sequential cosimulation method to integrate reliable field data and the posterior probability data generated by the maximum likelihood preclassification, and, thus, obtained more continuous forest covers in final classification. Recently, Li *et al.* [32] used a MCRF cosimulation (coMCRF) model and expert-interpreted sample data to postprocess the preclassified image data generated by a

Manuscript received April 17, 2016; revised May 16, 2016 and June 19, 2016; accepted July 23, 2016. Date of publication August 14, 2016; date of current version February 13, 2017. This work was supported in part by the U.S. National Science Foundation under Grant 1414108. *(Corresponding author: Weidong Li.)*

The authors are with the Department of Geography and Center for Environmental Sciences and Engineering, University of Connecticut, Storrs, CT 06269 USA (e-mail: weixing.zhang@uconn.edu; weidongwoody@gmail.com; zhangchuangrong@gmail.com; xiaojiang.li@uconn.edu).

Color versions of one or more of the figures in this paper are available online at http://ieeexplore.ieee.org.

Digital Object Identifier 10.1109/JSTARS.2016.2596040

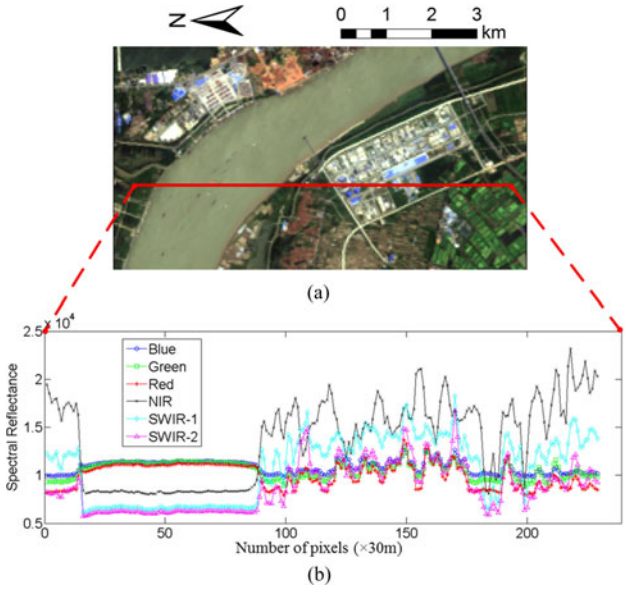

Fig. 1. North-south directional remotely sensed image spectral cross section in Wuhan city. (a) Line of pixels along the red line. (b) Corresponding spectral reflectance values of pixels of six bands along the line.

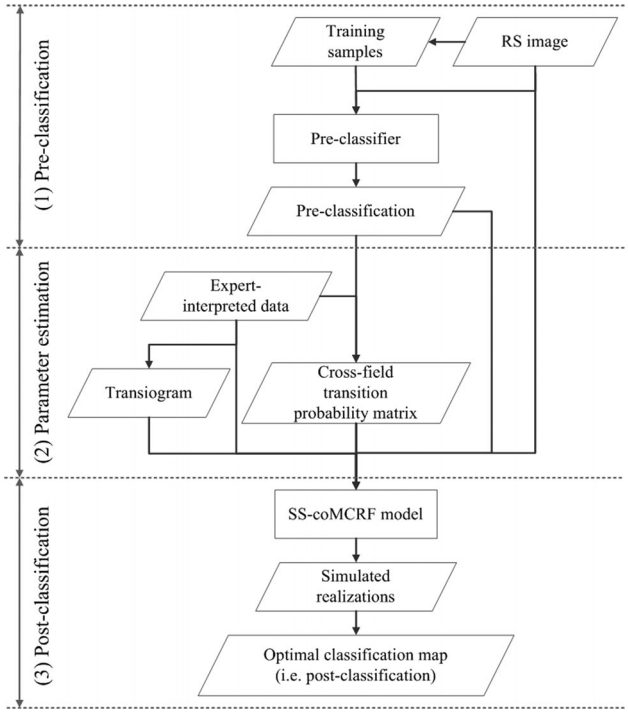

Fig. 2. Flowchart for the whole procedure from preclassification to final post-classification results using the SS-coMCRF model.

conventional classifier to increase the classification accuracy of land cover classes. However, the geometric features of land cover objects are difficult to be reproduced by geostatistical methods that traditionally use two-point statistics and circular neighborhoods [33]. It seems that use of multiple-point statistics may solve this problem to some extent, but it only can approximately reproduce the known and relatively simple patterns provided by a fed training image (see [34]). In order to reduce the smoothing effect caused by the neighborhoods used in geostatistical models, incorporating spectral dissimilarity of pixels between different classes and spectral similarity of pixels within the same class as spatial constraints in land cover postclassification should be promising.

Spectral similarity measures have been widely used in image classification, especially in hyperspectral image classification [35]–[37], because pixels belonging to the same land cover class are more likely to have similar spectral features. Some of the most popularly used spectral similarity measures are spectral angle measure (SAM), Euclidean distance measure (EDM), spectral correlation measure (SCM) (i.e., Pearson correlation coefficient), and spectral information divergence (SID). In this study, Jaccard index (also known as Jaccard similarity coefficient) and SCM, which are mutually complementary, were used to measure spectral similarity between two pixels, and used as spatial constraints to enhance the geometric features of land cover classes in postclassification, because spectral reflectance tends to be similar for pixels belonging to the same class in real world at a local scale but change dramatically with class changes along a direction (see Fig. 1). The objective of this study is to incorporate the spectral similarity measures into the coMCRF model, that is, to propose a spectral similarity-enhanced coMCRF (SS-coMCRF) model, for reducing the geometric information loss of land cover objects in postclassification. In case studies, NN classifier and SVM classifier were used for preclassification. To examine the performance of the SS-coMCRF model, we compared it with the coMCRF model using expert-interpreted sample datasets with different sample densities in two case studies. Here, expert-interpreted sample data refer to the pixel label data discerned by expert judgment based on professional insight and integrative information from multiple sources (e.g., various high resolution images, Google Earth historical images, and existing land use maps).

II. Methods

NN classifier and SVM classifier were used separately to make preclassifications. For conducting preclassifications, representative samples were selected manually from the original images as training data. The same training samples were fed to both classifiers to generate preclassified images. Then, coMCRF and SS-coMCRF were used, respectively, to postprocess the preclassified images. The NN classifier and SVM classifier modules of the ENVI software were used in this study. Both coMCRF and SS-coMCRF models were implemented by Python programs. A flowchart in Fig. 2 shows the general algorithm from preclassification to final postclassification results using the SS-coMCRF model.

A. Preclassifiers

NN classifier is designed to work like an animal's brain. Basically, two common learning paradigms, that is, the least-mean-square algorithm and the error back-propagation algorithm, may be used in the NN classifier. In this study, the latter was employed. Unlike the maximum likelihood or other statistical methods, NN is a nonparametric and distribution-free classification algorithm. In addition, there is no requirement for *a priori* knowledge of the statistical characteristics of the preset

classes [6], [7], [38]. Furthermore, the capability of learning and adaptively simulating complicated information makes this method capable to deal with various types of remotely sensed data, including high-resolution images [39]. However, the closed operation in the hidden layer makes NN work like a black box so that things behind are difficult to be well understood [20], [40]. In this study, NN was implemented with one hidden layer and a thousand training iterations.

SVM classifier is another advanced supervised classifier used in classification of remotely sensed imagery, based on machine-learning algorithms, such as NN [2]. The original SVM is a binary classifier. However, the distinction of multiple classes gets involved in most remotely sensed image classifications. Thus, multiple SVMs are needed to classify an image. Two combined multiple SVM classifiers are used commonly. One is called the "one against all" approach, which means a bunch of binary classifiers are used to separate one class from the rest. The other is called the "one against one" approach, which means that a series of classifiers are applied to each pair of classes [41], [42]. The SVM classifier has great performance in nonlinear classifications with help of a kernel function, similar to that in linear classifications. To some extent, the performance of SVM relies on the selection of the kernel function, its parameters, and soft marginal parameters [2]. In this study, SVM with the pairwise classification strategy (i.e., the "one against one" approach) was employed.

B. Markov Chain Random Field Cosimulation Model

The Bayesian coMCRF model extends the MCRF model based on the MCRF theory, which was initially proposed by Li [43] as the supporting theory for Markov chain geostatistics and further described with emphasis of the sequential Bayesian updating view in [32] and [44]. The local conditional probability distribution of the MCRF at any unobserved location is decided by sequential Bayesian updating over the prior probability using each of the nearest data within a neighborhood as new evidence. The MCRF local conditional probability function for a specific unobserved location $\mathbf{u}_0$ is described as

$$\begin{aligned} & p\left[i_0\left(\mathbf{u}_0\right)\left|i_1\left(\mathbf{u}_1\right), \ldots, i_m\left(\mathbf{u}_m\right)\right.\right] \\ & \quad = p\left[i_m\left(\mathbf{u}_m\right)\left|i_0\left(\mathbf{u}_0\right), \ldots, i_{m-1}\left(\mathbf{u}_{m-1}\right)\right.\right] \ldots p\left[i_2\left(\mathbf{u}_2\right)\right. \\ & \qquad \left.\left|i_0(\mathbf{u}_0), i_1(\mathbf{u}_1)\right.\right] \cdot \frac{p[i_0(\mathbf{u}_0)\left|i_1(\mathbf{u}_1)\right.]}{p\left[i_1\left(\mathbf{u}_1\right), \ldots, i_m(\mathbf{u}_m)\right] / p[i_1\left(\mathbf{u}_1\right)]} \end{aligned} \tag{1}$$

where i_1 to i_m are the states of the *m* nearest neighbors around the unobserved location $\mathbf{u}_0$; the left-hand side of the equation is the posterior probability of state (or class) i_0 at the location $\mathbf{u}_0$; the denominator in the right-hand side is a constant; $p[i_0(\mathbf{u}_0)|i_1(\mathbf{u}_1)]$ represents the prior probability; and the left portion of the right-hand side are likelihood functions for updating the prior probability. Based on the quantitative relationship $p[i_0(\mathbf{u}_0)|i_1(\mathbf{u}_1)] = p[i_1(\mathbf{u}_1)|i_0(\mathbf{u}_0)] \times p[i_0(\mathbf{u}_0)]/p[i_1(\mathbf{u}_1)]$, it is also feasible to use $p[i_0(\mathbf{u}_0)]$ as the prior probability; then there will be one more likelihood function $p[i_1(\mathbf{u}_1)|i_0(\mathbf{u}_0)]$ in (1).

Assuming conditional independence of nearest data within a neighborhood [43] and using the transiogram notation [45], as well as applying the total probably law, the above (1) is simplified to

$$\begin{aligned} & p\left[i_0\left(\mathbf{u}_0\right)\left|i_1\left(\mathbf{u}_1\right), \ldots, i_m\left(\mathbf{u}_m\right)\right.\right] \\ & \quad = \frac{p_{i_1 i_0}\left(\mathbf{h}_{10}\right) \prod_{g=2}^{m} p_{i_0 i_g}\left(\mathbf{h}_{0g}\right)}{\sum_{f_0=1}^{n}\left[p_{i_1 f_0}\left(\mathbf{h}_{10}\right) \prod_{g=2}^{m} p_{f_0 i_g}\left(\mathbf{h}_{0g}\right)\right]} \end{aligned} \tag{2}$$

where n is the number of classes, and $p_{i_0 i_g}(\mathbf{h}_{0g})$ is a specific transition probability over the distance lag $\mathbf{h}_{0g}$, which can be fetched from a transiogram model $p_{i_0 i_g}(\mathbf{h})$. The sequential Bayesian updating idea and the conditional independence assumption for spatial data were recently also used in a spatial model for semantic segmentation of remote sensed imagery [46].

To approximately meet the conditional independence condition of nearest data, the MCRF model uses a quadrantal neighborhood, which considers only one nearest datum from each quadrant that sectors the neighborhood (see Fig. 3) [47]. The coMCRF model for improving land cover classification considers the colocated datum of a preclassified image that serves as a covariate field. Therefore, the coMCRF model used here is given as

$$\begin{aligned} & p\left[i_0\left(\mathbf{u}_0\right)\left|i_1\left(\mathbf{u}_1\right), \ldots, i_4\left(\mathbf{u}_4\right); r_0\left(\mathbf{u}_0\right)\right.\right] \\ & \quad = \frac{q_{i_0 r_0} p_{i_1 i_0}\left(\mathbf{h}_{10}\right) \prod_{g=2}^{4} p_{i_0 i_g}\left(\mathbf{h}_{0g}\right)}{\sum_{f_0=1}^{n}\left[q_{f_0 r_0} p_{i_1 f_0}\left(\mathbf{h}_{10}\right) \prod_{g=2}^{4} p_{f_0 i_g}\left(\mathbf{h}_{0g}\right)\right]} \end{aligned} \tag{3}$$

where $q_{i_0 r_0}$ represents the cross-field transition probability from class i_0 at the location $\mathbf{u}_0$ in the primary categorical field being simulated to class r_0 at the colocation in the covariate field of the preclassified image [32].

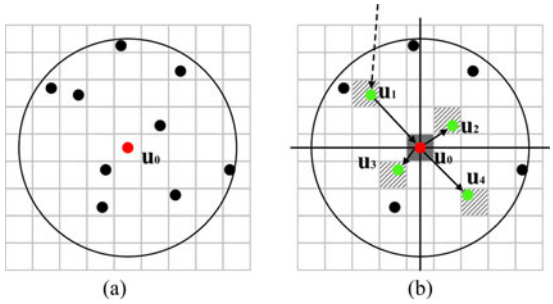

Fig. 3. Quadrantal MCRF neighborhood under the conditional independence assumption of nearest data. (a) Search area for seeking nearest neighbors to estimate the class of land cover at the uninformed central point $\mathbf{u}_0$. (b) Sectored neighborhood, which considers one nearest datum from each quadrant if one datum can be found from the quadrant. Black solid dots: informed data (sample data or previously simulated data). Red dot: the uninformed pixel being estimated. Green dots: selected nearest data for the neighborhood. Arrows represent transition probability directions (see [32]).

C. Spectral Similarity Measures

There are mainly two groups of spectral similarity measures: deterministic measures and stochastic measures [35], [48]. SAM, EDM, and SCM belong to deterministic measures, and SID is one of stochastic measures. Jaccard index, which was rarely used in remote sensing, should also belong to

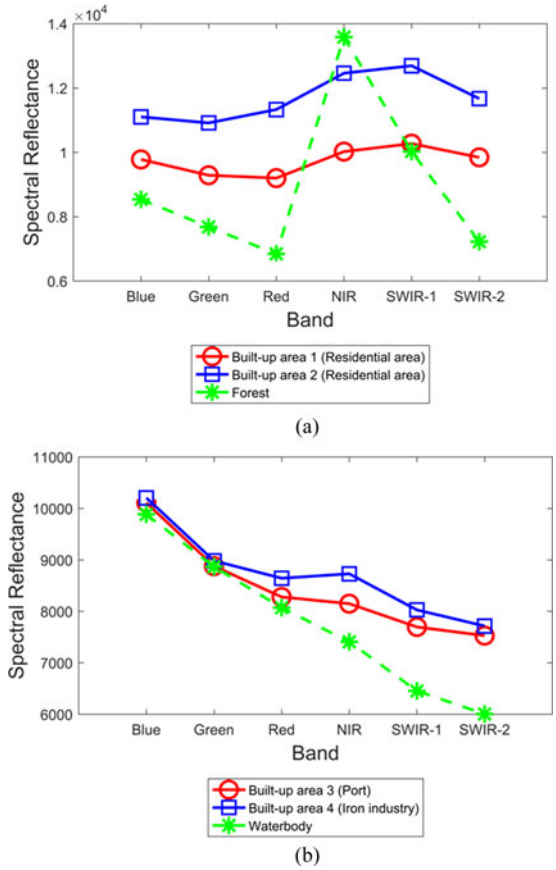

Fig. 4. Examples of spectral reflectance value vectors at different sample locations, for demonstrating the characteristics of the Jaccard index and SMC in distinguishing different land cover classes. (a) Spectral reflectance value vectors of three sample pixels for built-up areas 1 and 2 (both are residential areas) and forest. (b) Spectral reflectance value vectors of three sample pixels for built-up area 3 (port), built-up area 4 (iron industry), and waterbody.

deterministic measures. After testing these measures separately and pairwise in the coMCRF model, we found that using the two mutually complementary measures, Jaccard index and SCM (see Fig. 4), as an integrated constraining factor had the best effect in terms of both computational efficiency and better capture of geometric shapes. Thus, Jaccard index and SCM were used as spectral similarity measures to construct the integrated constraining factor in the proposed SS-coMCRF model.

1) Jaccard Index: Jaccard index [49] is one of the metrics used to measure the similarity, dissimilarity, and distance of two sample sets [50], which is defined as the ratio of the region of the intersection to the region of the union of two sample sets

$$\boldsymbol{J}\ (A,B) = \frac{|A \cap B|}{|A \cup B|} \tag{4}$$

where A and B are two sample sets for comparison. Practically, given two spectral vectors $\boldsymbol{x} = (x_1, x_2, \ldots, x_n)$ and $\boldsymbol{y} = (y_1, y_2, \ldots, y_n)$ with all $x_i, y_i \geq 0$, to estimate their spectral similarity, their Jaccard index is described as

$$\boldsymbol{J}\ (\boldsymbol{x},\boldsymbol{y}) = \frac{\sum_i \min(x_i,\ y_i)}{\sum_i \max(x_i,\ y_i)} \tag{5}$$

where max and min are pointwise maximum operator and pointwise minimum operator, respectively.

The drawback of Jaccard index is that it only responds to vector differences in magnitude. Thus, it is incapable of distinguishing between two classes if their spectral value vectors have very different shapes but similar magnitudes. To deal with this problem, SCM is applied to complement the Jaccard index to measure spectral similarity. SCM is a commonly used measure for the linear relationship between two random variables [35], but SCM also has its intrinsic drawback—it will fail if the shapes of two vectors are similar but their magnitudes are largely different [51]. For example, in Fig. 4(a), the Jaccard index value between built-up area 1 and built-up area 2 is 0.8123, and the Jaccard index value between built-up area 1 and forest is 0.8323. These two values are very close, which means Jaccard index is incapable of distinguishing forest out of built-up area. However, the SMC value of built-up area 1 and built-up area 2 is 0.8320, and the SMC value between built-up area 1 and forest is 0.6464. These two values have much larger difference, which means that SMC is capable of identifying forest out of built-up area in this case. On the contrary, in Fig. 4(b), the SMC value between built-up area 3 and built-up area 4 is 0.9826, and the SMC value between built-up area 3 and waterbody is 0.9565. These two values are very close, which means SMC is incapable of distinguishing waterbody out of built-up area. However, the Jaccard index value of built-up area 3 and built-up area 4 is 0.9682, and the Jaccard index value between built-up area 3 and waterbody is 0.8927. These two values have larger difference in comparison with the SMC values, which means that Jaccard index is capable of identifying waterbody out of built-up area.

2) Spectral Correlation Measure: The SCM is able to reflect the relationship between two vectors. Given two vectors $\boldsymbol{x} = (x_1, x_2, \ldots, x_n)$ and $\boldsymbol{y} = (y_1, y_2, \ldots, y_n)$ with all $x_i, y_i \geq 0$, the SCM $\boldsymbol{\rho_{xy}}$ of vectors $\boldsymbol{x}$ and $\boldsymbol{y}$ is defined as

$$\boldsymbol{\rho}_{\mathrm{xy}} = \frac{C_{\mathrm{xy}}}{\sqrt{C_{\mathrm{xx}} \cdot C_{\mathrm{yy}}}} \tag{6}$$

where C_{xy} is the covariance of vectors $\boldsymbol{x}$ and $\boldsymbol{y}$, C_{xx} is the variance of vector $\boldsymbol{x}$, and C_{yy} is the variance of vector $\boldsymbol{y}$. Here, we have $\boldsymbol{\rho}_{\mathrm{xy}} \in [-1, +1]$, where $+1$ means totally positive correlation, 0 means no correlation, and -1 means totally negative correlation. In measuring the linear relationship between two spectral vectors, negative SMC values generally are discarded [35]. In this case, in order to simplify the computation complexity, negative SMC values are replaced by 0.01 as the similarity percentage of two spectral vectors due to their apparent spectral dissimilarity.

D. Similarity-Enhanced coMCRF

At a *regional* scale (e.g., a whole study area), the spectral reflectance values of two pixels located distantly may be dissimilar even though they belong to the same class (see Fig. 5). This is one reason why traditional spectral-based classifiers cannot perform well when they are applied to some complex situations. Spatial statistical models have the capability to incorporate spatial correlation information into classification.

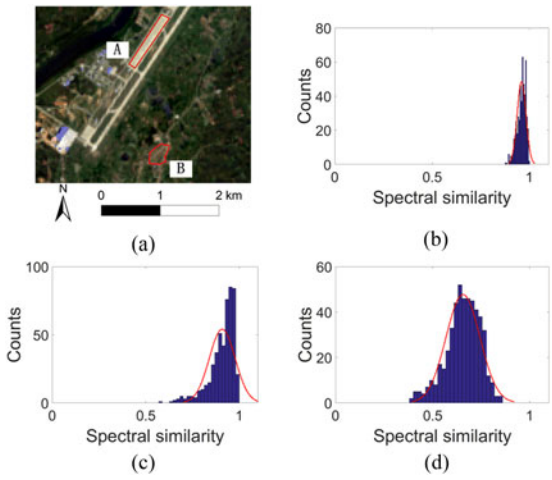

Fig. 5. Illustrating the spectral similarity of pixels of the same land cover class at a regional scale and at a local scale, calculated using the integrated constraining factor given in (7). (a) Two marked built-up areas A and B. (b) Histogram of spectral similarity between pixels within area A. (c) Histogram of spectral similarity between pixels within area B. (d) Histogram of spectral similarity between pixels from area A and pixels from area B. For each histogram, 500 pairs of pixels were selected randomly for calculating their similarity values. The spectral reflectance values of pixels in area A and those in area B tend to be dissimilar even though they belong to the same class, but the spectral reflectance values of pixels within area A or within area B tend to be similar.

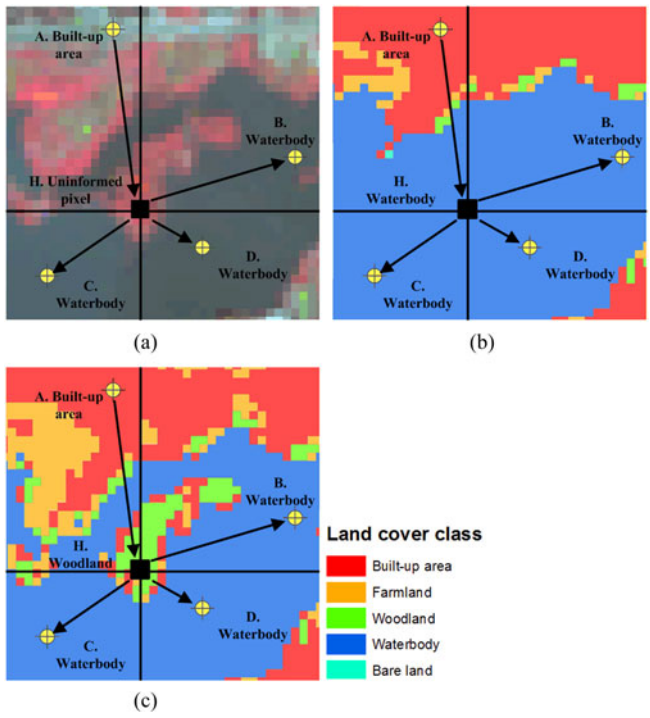

Fig. 6. Illustrating how the spectral similarity-based constraining factor helps us to estimate the class of an uninformed pixel (H) on an island using the four nearest pixel data–A, B, C, and D (note that the co-located datum of the preclassified image is not shown) and the spectral values of the original image at the five pixels. (a) Four nearest data (A, B, C, and D) and the original false color image (background) for estimating the class of the label-uninformed pixel H. (b) Because three of the four nearest informed pixels belong to the waterbody class, the uninformed pixel is more likely reclassified as waterbody in the coMCRF model. (c) After the spectral similarity-based constraining factor is applied, the estimated probability of pixel H to be waterbody becomes very low, and, consequently, pixel H has much more possibility to be reclassified as other classes such as woodland in postclassification.

However, due to the impact of spatial data within a usually circular neighborhood, geostatistical models tend to have the smoothing effect that usually ignores or removes the geometric features of classes (e.g., narrow linear features, regular linear/curvilinear boundaries) while eliminating the noise and some details in the classified images. In order to reduce the geometric feature loss caused by the smoothing effect, a spectral similarity-based constraining factor is added to modify the coMCRF model for land cover postclassification.

The constraining factor is based on the following understanding: At a *local* scale (e.g., a neighborhood area or the area of a land cover object), the spectral reflectance values of two pixels tend to be similar if they belong to the same class in real world (see Fig. 5), but they tend to be very different if they belong to different classes in real world. Thus, when a transition probability for a neighborhood involves two different classes (i.e., cross transition), the constraining factor is assigned to 1.0; but when a transition probability involves the same class (i.e., autotransition), the constraining factor is applied to update the transition probability in estimating the local probability distribution. By this way, the contribution of the spectrally similar nearest data is enhanced and the contribution of the spectrally dissimilar nearest data is reduced.

For example, in Fig. 6, four nearest data (A, B, C, and D) are used to estimate the class of the label-uninformed pixel H. Due to the sparsity of data points in the area, there is no data point located on the island. Because three of the four nearest informed pixels belong to the waterbody class, the uninformed pixel is more likely reclassified as waterbody in the coMCRF model. However, after the spectral similarity-based constraining factor is applied, the transition probabilities involving the three waterbody pixels in the SS-coMCRF model have to be multiplied by a very small factor value when estimating the probability of pixel H to be waterbody, because the spectral value of pixel H is very different from the spectral values of the waterbody pixels B, C, and D in the original image. Thus, the estimated probability of pixel H to be waterbody becomes very low, and, consequently, pixel H has much less possibility to be reclassified as waterbody and has more possibility to be reclassified as other classes in postclassification. The spectral similarity-based constraining factor, therefore, is helpful to capture the geometric features and some details of land cover objects by emphasizing the spectral similarity of pixels of the same class and the spectral dissimilarity of pixels of different classes within a neighborhood when estimating an uninformed pixel using its nearest data neighbors.

The spectral similarity-based constraining factor, which comprises the Jaccard index given in (5) and the SCM given in (6), is expressed as

$$\boldsymbol{S}_{i_l i_k} = \begin{cases} 1.0, & i_l \neq i_k \\ \boldsymbol{\rho}_{i_l i_k}\left(x_l, y_k\right) \cdot \boldsymbol{J}_{i_l i_k}\left(x_l, y_k\right), & i_l = i_k \end{cases} \tag{7}$$

where i_l is the land cover class of pixel $\boldsymbol{l}$; $\boldsymbol{\rho}_{i_l i_k}$ and $\boldsymbol{J}_{i_l i_k}$ are the SCM and the Jaccard index of the spectral vectors (i.e., spectral

values of different bands) of pixel $\boldsymbol{l}$ and pixel $\boldsymbol{k}$, respectively ($\boldsymbol{x}_l$ and $\boldsymbol{y}_k$ are spectral vectors of pixel $\boldsymbol{l}$ and pixel $\boldsymbol{k}$, respectively). With incorporation of the constraining factor, the similarity-enhanced coMCRF (i.e., SS-coMCRF) model is consequently given as

$$p\left[i_0\left(\mathbf{u}_0\right)|i_1\left(\mathbf{u}_1\right),\ldots,\ i_4\left(\mathbf{u}_4\right);r_0\left(\mathbf{u}_0\right);Spectra\right] = \frac{q_{i_0 r_0} p_{i_1 i_0}\left(\mathbf{h}_{10}\right) \boldsymbol{S}_{i_1 i_0} \prod_{g=2}^{4} p_{i_0 i_g}\left(\mathbf{h}_{0g}\right) \boldsymbol{S}_{i_0 i_g}}{\sum_{f_0=1}^{n}\left[q_{f_0 r_0} p_{i_1 f_0}\left(\mathbf{h}_{10}\right) \boldsymbol{S}_{i_1 f_0} \prod_{g=2}^{4} p_{f_0 i_g}\left(\mathbf{h}_{0g}\right) \boldsymbol{S}_{f_0 i_g}\right]}. \tag{8}$$

III. Data and Experiments

A. Image Data

One study area is located in Wuhan, China. A medium-resolution (Landsat 8 OLI) image for Wuhan city, acquired on September 17, 2013, was used in this study (downloaded using USGS EarthExplorer from www.earthexplorer.usgs.gov). There are total 11 bands in the Landsat 8 OLI imagery, including all of the bands (blue, green, red, near infrared, short-wave infrared 1, and short-wave infrared 2) from previous Landsat missions other than some new ones. New band 1 (coastal aerosol) is designed for coastal and aerosol studies and new band 9 (cirrus) is designed for cirrus cloud detection [52]. Band 8 is panchromatic with a resolution of 15 m. Bands 10 and 11 (thermal infrared) are for surface temperature detection with a resolution of 100 meters. Therefore, six spectral bands (band 2 to band 7) of the image were stacked for preclassification. A scene of 1000 × 1000 pixels with a spatial resolution of 30 m, which covers the northeastern part of Wuhan with an area of 90 000 ha, was clipped from the image as the study area (see Fig. 7(a)). This study area has a relatively heterogeneous and complex landscape, which is composed of urban areas, suburb areas, agricultural lands, rivers, hills, woodlands, and many water bodies (lakes and ponds), with rugged topography. For this study, five major land cover classes were mapped in the study area, namely built-up area (C1), farmland (C2), woodland (C3), waterbody (C4), and bare land (C5).

The other study area is located in Shenzhen, China. A scene (see Fig. 7(b)) of 1134×1169 pixels with a spatial resolution of 0.6 m, extracted from a Quickbird satellite image, acquired on April 26, 2012, was used. There are four channels in the Quickbird satellite imagery, including blue (450–520 nm), green (520–600 nm), red (630–690 nm), and near-IR (760–890 nm). The image used in this case study was downloaded under the Ortho Ready Standard (i.e., four-band pan-sharpened) from DigitalGlobe (www.digitalglobe.com). This scene is mostly located in the urban area of Shenzhen. Therefore, five land cover classes, including impervious surface (T1), trees/shrubs (T2), grass/lawn (T3), waterbody (T4), and sand/soil (T5) were considered for this case study.

B. Expert-Interpreted Data

Preclassification data and expert interpreted data are two of the needed data sets for performing postclassification using coMCRF and SS-coMCRF. In this experiment, to test the proposed SS-coMCRF model, expert-interpreted data were discerned for each study area by expert judgment based on professional insight and integrative information from multiple sources (high-resolution images and other reliable reference data, such as Bing maps and Google Earth historical images).

For the study area in Wuhan, a relatively dense dataset (3215 sample points, 0.32% of the total image pixels) and a relatively

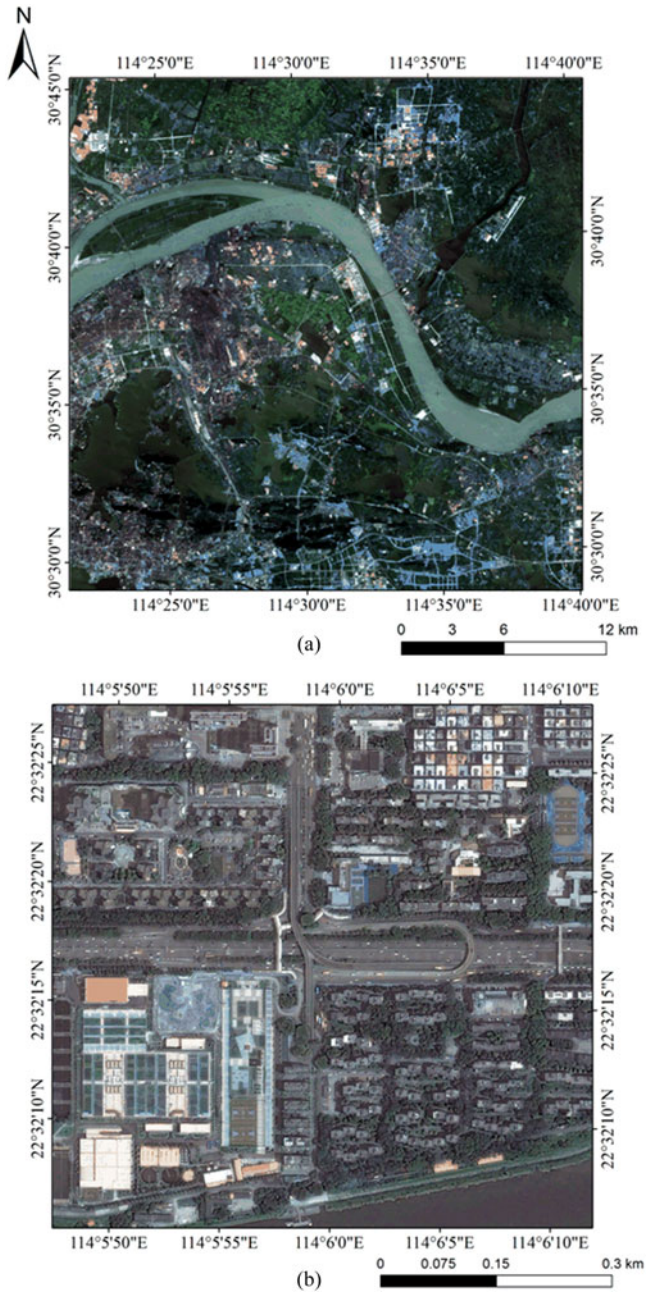

Fig. 7. Study areas for the two case studies. (a) Landsat 8 OLI true color image (R: red, G: green, B: blue) for the study area in Wuhan, China, acquired on September 17, 2013, with a pixel size of 30 m × 30 m. The coordinates (latitude, longitude) of the upper left corner are (30°45′04″N, 114°22′13″E). (b) QuickBird true color image (R: red, G: green, B: blue) for the study area in Shenzhen, China, acquired on April 26, 2012, with a pixel size of 0.6 m × 0.6 m. The coordinates of the upper left corner are (22°32′27.40″N, 114°5′47.23″E).

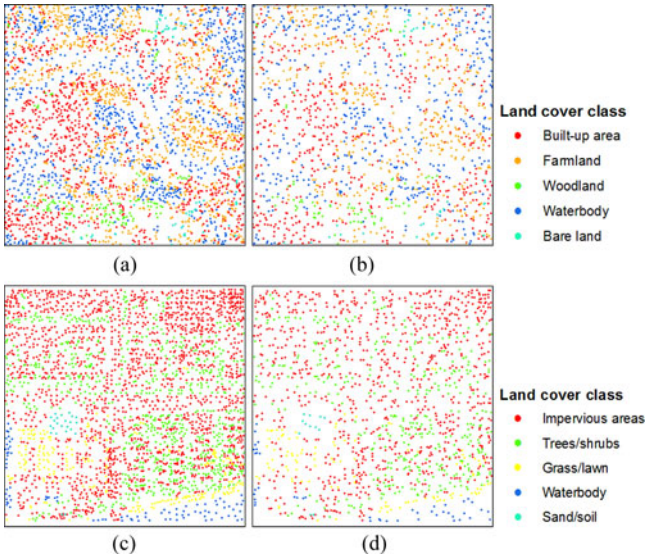

Fig. 8. Expert-interpreted land cover sample datasets for the study areas in Wuhan and Shenzhen. (a) and (b) Dense dataset and sparse dataset for the Wuhan study area. (c) and (d) Dense dataset and sparse dataset for the Shenzhen study area.

TABLE I
QUANTITIES OF EXPERT-INTERPRETED SAMPLE DATASETS, TEST DATA, AND TRAINING DATA FOR THE TWO CASE STUDIES

Case	Class	Expect-interpreted sample data (pixel)		Test data (pixel)	Training data (pixel)
		Dense	Medium		
Wuhan	C1	1114	557	280	470
	C2	997	498	250	331
	C3	142	72	35	88
	C4	889	444	222	333
	C5	73	36	19	60
	Total	3215	1607	806	1282
Shenzhen	T1	1748	874	438	1380
	T2	738	368	184	919
	T3	217	109	54	331
	T4	90	45	23	157
	T5	23	12	5	112
	Total	2816	1408	704	2899

sparse dataset (1607 sample points, 0.16% of the total image pixels), all expert-interpreted from multiple sources, were used as hard conditioning data and for estimation of transiograms and cross-field transition probability matrix used in cosimulations (see Fig. 8(a) and (b)). For the study area in Shenzhen, a relatively dense dataset (2816 sample points, 0.21% of the total image pixels) and a relatively sparse dataset (1408 sample points, 0.11% of the total image pixels) were interpreted for the same purposes (see Fig. 8(c) and (d)). Cosimulations were consequently conducted on corresponding expert-interpreted sample datasets with transiogram models, cross-field transition probability matrix, and preclassification data for each case study. In addition, the original image for preclassification is needed by SS-coMCRF for providing pixel spectral data for similarity measure computation in each postclassification.

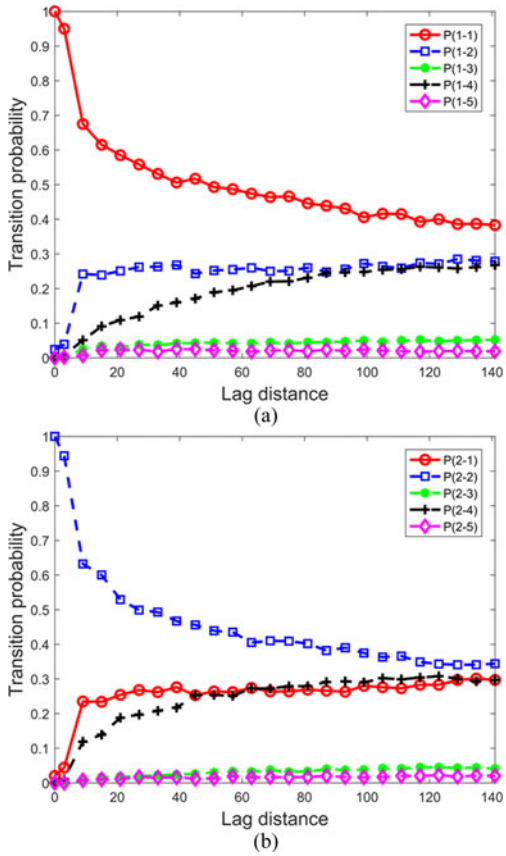

Fig. 9. Two subsets of transiogram models estimated from the expert-interpreted dense sample data set for the Wuhan case study. Class 1 is built-up area, class 2 is farmland, class 3 is woodland, class 4 is waterbody, and class 5 is bare land. P (1–4) denotes the transition probability from built-up area to waterbody. Lag distance is the separate distance between a pair of data points.

Specific quantities of expert-interpreted sample data, test data, and training data of each land cover class for the two study areas are shown in Table I. The test data are also expert-interpreted data from multiple sources, but they were used only for validating the preclassification and postclassification results. The training data are different, because for each study area they were selected only from the corresponding original image so that they may reflect the image's spectral characteristics and they were used only for preclassification of land cover classes from the original image.

C. Parameter Estimation

Besides expert-interpreted sample data and preclassified image data, two sets of parameter data—a set of transiogram models and a cross-field transition probability matrix are required in each coMCRF [32]. Transiogram models represent the spatial auto and cross correlations of classes in the categorical field to be simulated and can be inferred from experimental transiograms directly estimated from sample data [45]. Considering that the expert-interpreted sample data are usually sufficient to generate reliable experimental transiograms, a simple linear interpolation method [53] was used in this study to get transiogram models from experimental transiograms (see Fig. 9 for two subsects

TABLE II
CROSS-FIELD TRANSITION PROBABILITY MATRIX FROM CLASSES OF THE EXPERT-INTERPRETED DENSE SAMPLE DATASET TO CLASSES OF THE PRECLASSIFIED DATA BY THE NN CLASSIFIER FOR THE WUHAN CASE STUDY

		Cross-field transition probability				
	Class	Preclassified image				
		C1	C2	C3	C4	C5
Expert-interpreted dataset	C1	0.864	0.074	0.015	0.012	0.035
	C2	0.186	0.586	0.200	0.012	0.017
	C3	0.000	0.063	0.937	0.000	0.000
	C4	0.053	0.061	0.025	0.862	0.000
	C5	0.082	0.082	0.000	0.000	0.836

of transiogram models for the Wuhan study area). A cross-field transition probability matrix represents the correlations between classes of the categorical field to be simulated and the classes of a preclassified image, and can be simply estimated using the class transition frequencies from the sample dataset to their corresponding colocated data in the preclassified image [32] (see Table II for the cross-field transition probability matrix for the Wuhan study area).

The NN and SVM classifiers were used, respectively, to preclassify the selected remotely sensed images to obtain preclassified image datasets, which served as the covariate datasets in the coMCRF model and the SS-coMCRF model. A length of 50 pixels was used as the quadrantal neighborhood search radius, because for the sample datasets used in this study such a search radius can basically meet the requirement for finding a nearest datum in each quadrant of the neighborhood search area. Hundered simulated realizations were generated for each simulation, and an optimal classification map was further obtained based on the maximum probabilities estimated from each set of simulated realizations. The accuracy of each optimal classification map was calculated using the corresponding test sample dataset.

IV. RESULTS AND DISCUSSIONS

A. Classification Accuracy

Table II shows the estimated cross-field transition probability matrix for the NN preclassification and the expert-interpreted dense sample dataset for the Wuhan case study, which indicates that farmland was not well classified in the preclassification because 20% of those pixel locations that were interpreted as farmland by experts based on multiple available data sources were misclassified into woodland and 18.6% of them were misclassified into built-up area in preclassification mainly due to spectra confusion. This caused the low producer accuracy (57%) of farmland and the extremely low user accuracy (30%) of woodland in the preclassification map (see Table III). It is this kind of misclassifications that caused low producer accuracies of some classes, and, consequently, low user accuracies of some other related classes in preclassifications.

To evaluate the performance of the SS-coMCRF model, the accuracies of all preclassification maps and corresponding postclassification maps were calculated, as given in Table III for the Wuhan study area and in Table IV for the Shenzhen study area. The land cover postclassification maps by coMCRF and SS-coMCRF made obvious improvement in overall accuracy (OA) and Kappa coefficient (KC) over the corresponding preclassification maps by NN and SVM in all cosimulation cases, especially for the very high spatial resolution image for the Shenzhen case study.

For the Wuhan study area, SVM classifier generated higher preclassification OA and KC than NN classifier did; consequently, postclassifications by coMCRF and SS-coMCRF made less improvement over the SVM preclassification map than over the NN preclassification map (see Table III). Postclassification maps with dense sample datasets have apparently higher OAs and KCs than those with sparse datasets because dense sample datasets bring more accurate information into postclassifications. Comparing the postclassification maps generated by coMCRF and those generated by SS-coMCRF indicates that the two models performed similarly, with the latter being slightly better than the former (increasing OA by 0.0% to 1.5% and KC by 0.001 to 0.022). This means that the contribution of the spectral similarity measures to the overall postclassification accuracy is trivial. This is expected, because the use of spectral similarity measures in SS-coMCRF does not bring extra information for OA into postclassification—its purpose is to emphasize the contribution of the neighborhood data that have spectral values similar to that of the uninformed pixel being estimated while weakening the otherwise so as to reduce the smoothing effect of the coMCRF model.

For the Shenzhen case study, SVM classifier still performed better than NN classifier in preclassification; consequently, postclassification operations made more improvement over the NN preclassification maps in OA and KC than over the SVM preclassification maps (see Table IV). Similarly, postclassification maps with dense sample datasets have higher OAs and KCs than those with sparse datasets. However, comparing the postclassification maps generated by coMCRF and those generated by SS-coMCRF shows that for the very high-resolution mage, SS-coMCRF made slightly lower improvement than coMCRF did (decreasing OA by 0.7% to 2.4% and KC by 0.012 to 0.041). This means that the contribution of the spectral similarity measures to the overall postclassification accuracy can be negative sometimes, but the negative effect is still trivial.

For specific land cover classes, both coMCRF and SS-coMCRF postclassifications largely increased the very low producer or user accuracies of preclassified land cover classes (e.g., the producer accuracy of farmland and the user accuracies of woodland and bare land for the Wuhan case study with NN preclassifier; the producer accuracy of grass/lawn and the user accuracies of waterbody and sand/soil for the Shenzhen case study), while sometimes they reduced (often slightly) the high producer or user accuracies of some preclassified classes, especially when sample data are relatively sparse. Although some classes obtained relatively lower producer or user accuracies in postclassifications than they did in corresponding preclassifications, the negative effects are much less obvious in comparison with the positive effects achieved by postclassifications. In general,

TABLE III
ACCURACIES OF POSTCLASSIFICATION MAPS FOR THE WUHAN STUDY AREA BASED ON DIFFERENT EXPERT-INTERPRETED SAMPLE DATASETS AND THE PRECLASSIFIED IMAGE DATA BY NN AND SVM CLASSIFIERS

Method	Expert interpreted dataset		OA (%)	KC	Producer's Accuracy (%)					User's Accuracy (%)				
					Class									
					C1	C2	C3	C4	C5	C1	C2	C3	C4	C5
NN			76.6	0.678	88	57	89	83	79	81	79	30	96	48
NN + coMCRF	Dense	Value	86.4	0.807	81	90	94	88	89	92	74	85	97	94
		Improvement	9.8	0.128	−7	33	6	5	11	11	−4	55	0	46
	Sparse	Value	84.0	0.773	80	89	83	86	58	90	72	83	96	69
		Improvement	7.4	0.094	−8	32	−6	3	−21	9	−7	53	0	20
NN + SS-coMCRF	Dense	Value	86.6	0.811	80	94	94	86	89	94	75	80	97	85
		Improvement	10.0	0.132	−8	37	6	3	11	13	−4	50	1	37
	Sparse	Value	84.0	0.773	80	92	83	80	89	91	72	74	98	81
		Improvement	7.4	0.095	−7	35	−6	−3	11	9	−7	44	2	33
SVM			79.8	0.714	65	93	86	82	79	94	62	83	98	88
SVM + coMCRF	Dense	Value	84.5	0.781	78	83	91	94	84	90	75	80	92	80
		Improvement	4.7	0.067	12	−10	6	12	5	−4	12	−3	−7	−8
	Sparse	Value	82.0	0.745	76	81	89	91	58	88	73	84	88	69
		Improvement	2.2	0.031	11	−12	3	9	−21	−7	10	0	−10	−19
SVM + SS-coMCRF	Dense	Value	85.0	0.788	75	91	91	91	84	93	72	80	98	80
		Improvement	5.2	0.074	9	−2	6	9	5	−1	9	−3	0	−8
	Sparse	Value	83.5	0.766	73	92	86	88	68	92	69	83	98	72
		Improvement	3.7	0.053	8	−1	0	6	−11	−2	7	0	0	−16

TABLE IV
ACCURACIES OF POSTCLASSIFICATION MAPS FOR THE SHENZHEN STUDY AREA BASED ON DIFFERENT EXPERT-INTERPRETED SAMPLE DATASETS AND THE PRECLASSIFIED IMAGE DATA BY NN AND SVM CLASSIFIERS

Method	Expert interpreted data set		OA (%)	KC	Producer's Accuracy (%)					User's Accuracy (%)				
					Class									
					T1	T2	T3	T4	T5	T1	T2	T3	T4	T5
NN			79.8	0.661	83	83	39	96	60	99	78	68	24	15
NN + coMCRF	Dense	Value	96.2	0.929	97	95	91	100	80	99	94	79	100	100
		Improvement	16.3	0.268	14	12	52	4	20	0	16	11	76	85
	Sparse	Value	94.7	0.902	97	93	81	91	80	98	92	80	100	80
		Improvement	14.9	0.241	14	11	43	-4	20	-1	14	12	76	65
NN + SS-coMCRF	Dense	Value	93.8	0.888	93	96	89	100	80	100	93	77	100	22
		Improvement	13.9	0.227	10	13	50	4	20	0	15	10	76	7
	Sparse	Value	92.6	0.868	93	96	81	96	80	99	91	79	100	17
		Improvement	12.8	0.207	10	13	43	0	20	0	13	11	76	2
SVM			84.2	0.718	91	83	39	87	60	95	84	72	30	30
SVM + coMCRF	Dense	Value	95.3	0.913	98	91	85	96	80	98	94	79	100	100
		Improvement	11.1	0.195	8	9	46	9	20	2	11	7	70	70
	Sparse	Value	93.3	0.874	97	92	74	70	80	95	92	78	100	100
		Improvement	9.1	0.156	7	10	35	-17	20	0	8	6	70	70
SVM + SS-coMCRF	Dense	Value	94.6	0.901	96	93	89	96	80	99	91	79	100	57
		Improvement	10.4	0.183	5	11	50	9	20	3	8	6	70	27
	Sparse	Value	92.5	0.860	95	94	76	74	80	96	88	80	100	50
		Improvement	8.2	0.143	4	11	37	-13	20	1	5	8	70	20

while incorporating the spectral similarity measures into the coMCRF model for postclassification does not aim to improve the overall classification accuracy, it also does not obviously reduce or may even slightly improve the overall classification accuracy.

B. Improvement in Geometric Features

Comparing all of the postclassification maps with the corresponding NN and SVM preclassification maps can found that in addition to classification accuracy improvement (i.e., some

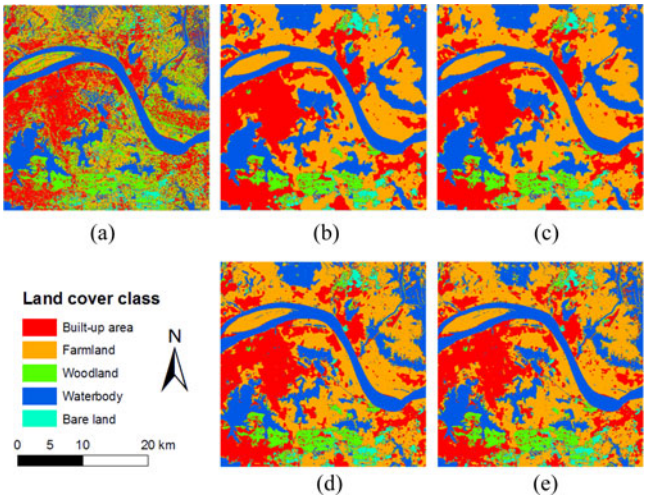

Fig. 10. Preclassification and postclassification results of the Landsat 8 OLI imagery for the Wuhan study area with the NN preclassifier. (a) NN preclassification map. (b) and (c) coMCRF postclassification maps based on the dense and sparse expert-interpreted datasets, respectively. (d) and (e) SS-coMCRF postclassification maps based on the dense and sparse expert-interpreted datasets, respectively.

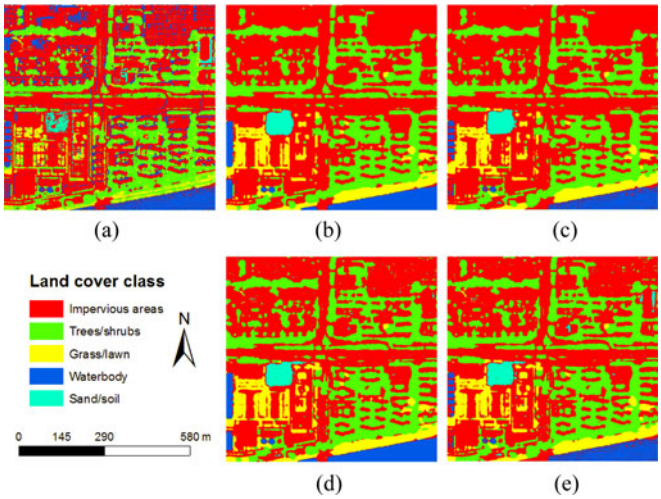

Fig. 12. Preclassification and postclassification results of the QuickBird imagery for the Shenzhen study area with the SVM preclassifier. (a) SVM preclassification map. (b) and (c) coMCRF postclassification maps based on the dense and sparse expert-interpreted datasets, respectively. (d) and (e) SS-coMCRF postclassification maps based on the dense and sparse expert-interpreted datasets, respectively.

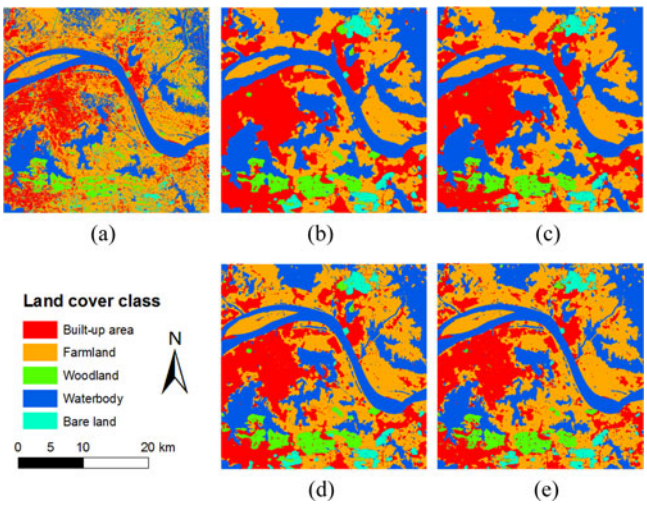

Fig. 11. Preclassification and postclassification results of the Landsat 8 OLI imagery for the Wuhan study area with the SVM preclassifier. (a) SVM preclassification map. (b) and (c) coMCRF postclassification maps based on the dense and sparse expert-interpreted datasets, respectively. (d) and (e) SS-coMCRF postclassification maps based on the dense and sparse expert-interpreted datasets, respectively.

misclassified pixels being corrected), coMCRF and SS-coMCRF postclassification maps have a common characteristic, which is essentially related to the smoothing effect of spatial statistical models. They all removed most "salt and pepper" noise that appeared in the preclassification maps, resulting in more continuous spatial patterns (see Figs. 10–12). This characteristic is especially obvious for the classification of the medium-resolution image for the Wuhan case study. This means that the two models have the filtering effect to noise. From Figs. 10 and 11 (for the Wuhan case study) and Fig. 12 (for the Shenzhen case study, preclassified by SVM classifier), one can see that lots of misclassified land cover labels (e.g., some farmlands were misclassified as woodlands, waterbodies with plants were misclassified as farmlands or woodlands, and boats on the river were misclassified as built-up areas, in Figs. 10(a) and 11(a); building shadows (mostly grass/lawn and impervious surface) were misclassified as waterbodies in Fig. 12(a)) and other noise that appear in the preclassified images were corrected in postclassified images.

However, there are apparent differences between the postclassified maps by coMCRF and those by SS-coMCRF. A typical difference is that the SS-coMCRF postclassification maps (see Fig. 10(d) and (e), Fig. 11(d) and (e), and Fig. 12(d) and (e)) show more linear features and more details, compared with the coMCRF postclassification maps (see Fig. 10(b) and (c), Fig. 11(b) and (c), and Fig. 12(b) and (c)), especially for the classification of the medium-resolution Landsat 8 OLI image for the Wuhan study area. It is worth to mention that relatively more land cover details could be preserved in postclassification maps when sample data used were sparser, although sparser sample data generally caused lower postclassification accuracies. This is because when conditioning sample data are sparser, the preclassified data play a relatively larger role in postclassification operation, thus bringing more features of the preclassification map into the final classification map.

To clearly demonstrate the advantage of the SS-coMCRF model in capturing the geometric shapes of some land cover objects, below we highlight a few of small subareas in postclassified maps. Fig. 13 shows the result maps of a small area around part of an island in Yangtze River in the Wuhan case study. In the preclassified image (see Fig. 13(a)) by the NN classifier, many places (mainly farmland) were mistakenly classified into woodland (also note that boats in the river were classified into small built-up areas). While coMCRF corrected the misclassified

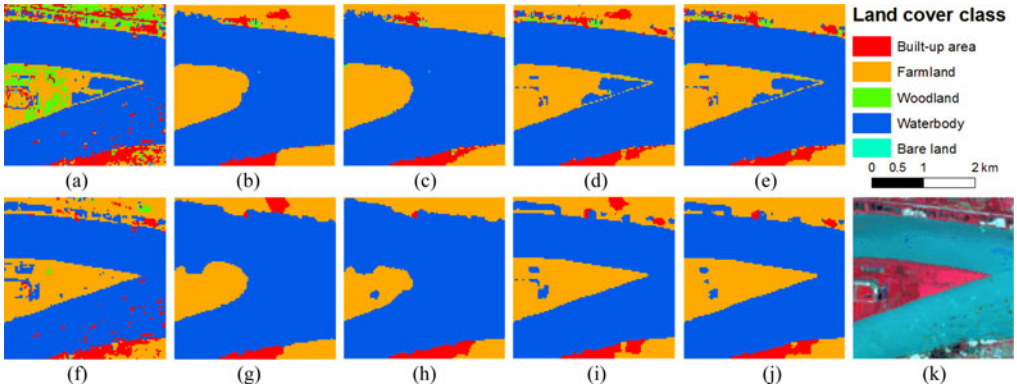

Fig. 13. Preclassification and postclassification results of a portion of the Landsat 8 OLI image for the Wuhan study area. (a) NN preclassification map. (b) and (c) coMCRF postclassification maps of NN preclassification, based on the dense and sparse datasets, respectively. (d) and (e) SS-coMCRF postclassification maps of NN preclassification, based on the dense and sparse datasets, respectively. (f) SVM preclassification map. (g) and (h) coMCRF postclassification maps of SVM preclassification, based on the dense and sparse datasets, respectively. (i) and (j) SS-coMCRF postclassification maps of SVM preclassification, based on the dense and sparse datasets, respectively. (k) Original false color image.

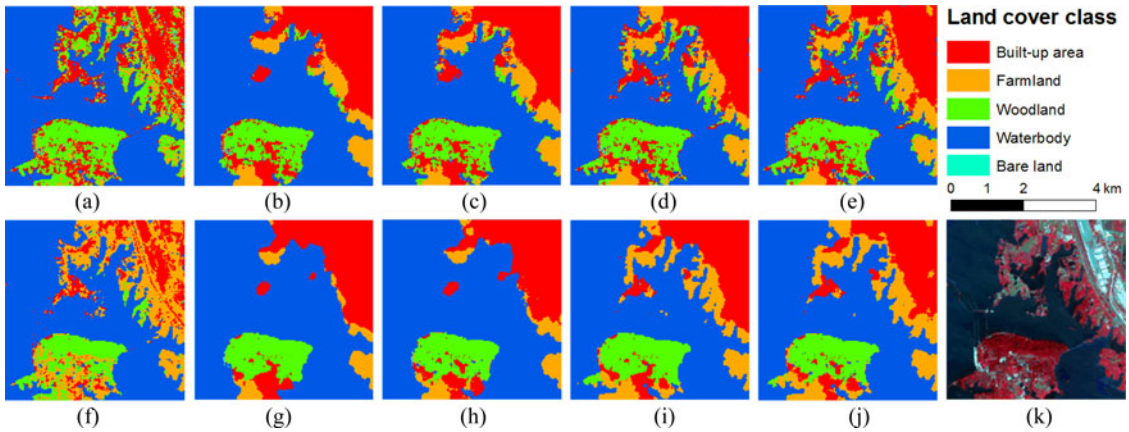

Fig. 14. Preclassification and postclassification results of a portion of the Landsat 8 OLI imagery for the Wuhan study area. (a) NN preclassification. (b) and (c) coMCRF postclassification maps of NN preclassification, based on the dense and sparse datasets, respectively. (d) and (e) SS-coMCRF postclassification maps of NN preclassification, based on the dense and sparse datasets, respectively. (f) SVM preclassification. (g) and (h) coMCRF postclassification maps of SVM preclassification, based on the dense and sparse datasets, respectively. (i) and (j) SS-coMCRF postclassification maps of SVM preclassification, based on the dense and sparse datasets, respectively. (k) Original false color image.

places in postclassification maps, it did not effectively capture the shape of the island due to its strong smoothing effect (see Fig. 13(b) and (c)). However, SS-coMCRF not only corrected the misclassified places in postclassification maps but also captured the geometric shapes of the island and upper river bank with more land cover details (see Fig. 13(d) and (e)). In the preclassified image (see Fig. 13(f)) by the SVM classifier, farmlands were not apparently misclassified, but boats were still misclassified as small built-up areas. While correcting the misclassified places, coMCRF strongly smoothed out the shape features of the island and upper river bank in postclassifications (see Fig. 13(g) and (h)). However, SS-coMCRF preserved the shapes of both the island and the upper river bank while it cleaned off the misclassified boats and other noise. In general, postclassification operations corrected misclassified land cover classes and removed noise due to the contribution of expert-interpreted sample data and spatial correlation information, thus improving the mapping accuracy; and the spectral similarity measures further helped to reduce the loss of geometric features and details of land cover objects in postclassification maps.

In the real world, spectral reflectance tends to be similar for pixels belonging to the same class but change dramatically between pixels belonging to different classes within a local area (see Fig. 1). Thus, incorporating spectral similarity measures into the coMCRF model for postclassification may reduce geometric feature loss of land cover objects, as shown in Figs. 10–12, as well as figures for highlighted subareas (see Figs. 13 to 15). Fig. 14 shows the preclassification and postclassification maps for the northeastern part of a large lake in the Wuhan study area. It can be seen that SS-coMCRF kept the complex lake boundary shapes and many details of terrestrial land cover classes along lake boundaries in postclassification maps (see Fig. 14(d), (e), (i), and (j)), while coMCRF smoothed out most of them (see Fig. 14(b), (c), (g), and (h)). Consequently, coMCRF seemingly overestimated the area of the lake by smoothing out the terrestrial boundary details, regardless of the density of sample data. Of course, because the preclassification maps generated by the NN classifier and the SVM classifier are quite different in nonwater classes, the corresponding postclassification maps also show some differences.

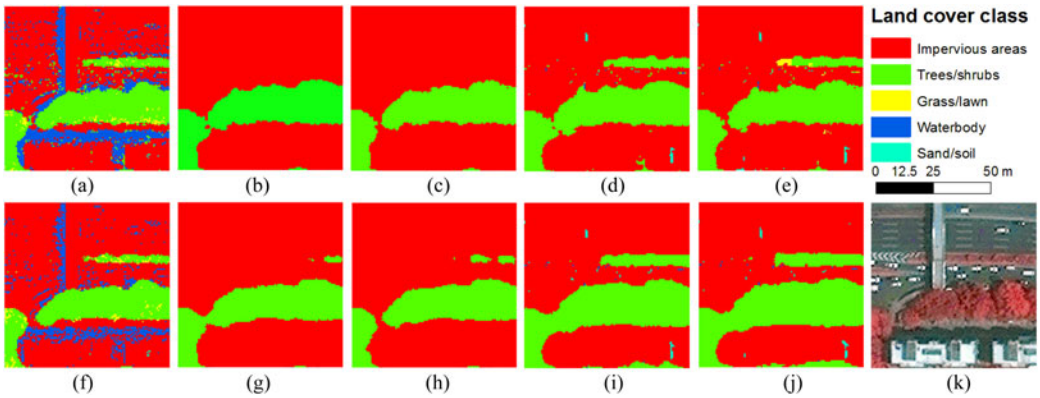

Fig. 15. Preclassification and postclassification results of a portion of the QuickBird image for the Shenzhen study area. (a) NN preclassification. (b) and (c) coMCRF postclassification maps of NN preclassification, based on the dense and sparse datasets, respectively. (d) and (e) SS-coMCRF postclassification maps of NN preclassification, based on the dense and sparse datasets, respectively. (f) SVM preclassification. (g) and (h) coMCRF postclassification maps of SVM preclassification, based on the dense and sparse datasets, respectively. (i) and (j) SS-coMCRF postclassification maps of SVM preclassification, based on the dense and sparse datasets, respectively. (k) Original false color image.

Fig. 15 shows that the false waterbodies in preclassification maps, which are mostly shadows on impervious surface and grass/lawn, were corrected in postclassifications for a small subarea in the Shenzhen study area. Such kind of misclassifications is very common for land cover classification in urban area from very high-resolution images. However, comparing the postclassification results from the coMCRF model and those from the SS-coMCRF model, one can see that the latter have less smoothing effects. A green stripe between the major driving road and the side road (see Fig. 15(k)) was smoothed out by coMCRF (see Fig. 15(b), (c), (g), and (h)) but preserved by SS-coMCRF (see Fig. 15(d), (e), (i), and (j)) in postclassification maps. The coMCRF model showed some tendency of overcorrecting the impervious surface class, while the SS-coMCRF model kept some noise as a tradeoff. The overcorrection tendency of coMCRF should be caused by the model's strong smoothing effects, which led to the local overestimation of impervious surface as a locally dominant land cover class.

C. Discussions

While correcting misclassified pixels, postclassification operation by the coMCRF model caused obvious smoothing effects in finally classified land cover maps, which not only remove noise but also smooth out most of linear features, tiny patches, and irregular patch boundaries, especially for medium-resolution classification. This is a common characteristic of spatial-dependence models. A major reason is that the local neighborhoods they used are normally composed of the nearest data within a circular search area that is usually much wider than many linear features or tiny objects. The second reason is that the postclassification maps shown above are all optimal maps (or map portions), of which each was based on the maximum occurrence probabilities estimated from a set of simulated realizations. Thus, the loss of geometric features of land cover objects is unavoidable because both the neighborhood structure and the optimization tend to remove fine features to get the general trend [33]. The incorporation of spectral similarity measures in postclassification helps to preserve the geometric shapes of real land cover objects to some extent, as demonstrated above in the postclassification maps by the SS-coMCRF model.

The filtering effect of incorporating data dependence should be the major reason causing the removal of noise and many small land cover patches. Because of the sparseness of expert-interpreted sample data (accounting for only 0.32% to 0.11% of total pixels for the dense and sparse datasets), estimation of the local conditional probability distribution of land cover classes at an unsampled pixel has to depend on the nearest sample data within a relatively large search area (e.g., a search radius of 50 pixels length) at the early simulation stage. Thus, the filtering effect on the preclassified pixel data can be strong. Although the smoothing effects can remove noise and increase connectivity, they also cause negative effects—removing narrow linear features and tiny land cover patches that may be correct.

The smoothing effect caused by optimization over a number of simulated realization maps is limited, because simulated realizations (see Fig. 16(a)–(d)) and the corresponding optimal classification maps (see Fig. 14(c) and (e)) have similar smoothing characteristics except that the former have some extra details (small patches). However, the occurrence probability maps of waterbody (see Fig. 16(e) and (f)) from the postclassification models show that SS-coMCRF generated less uncertainty than coMCRF did at class boundaries, while the former also captured much more land cover patch details than the latter did. This means that incorporating spectral similarity measures into land cover postclassification by using SS-coMCRF narrows the local-scale uncertainty space (i.e., increases the local-scale certainty), and, thus, contributes obviously to the geometric accuracy of land cover classes (e.g., waterbody), although it generally does not increase the OA of postclassification maps. The tradeoff for incorporating spectral similarity measures to reduce the geometric feature loss of land cover objects is that the postclassification maps by SS-coMCRF may keep some noise and some tiny land cover patches that may not be correctly classified. This tradeoff may be one reason why SS-coMCRF does not apparently improve or even slightly reduce the OA of postclassification maps.

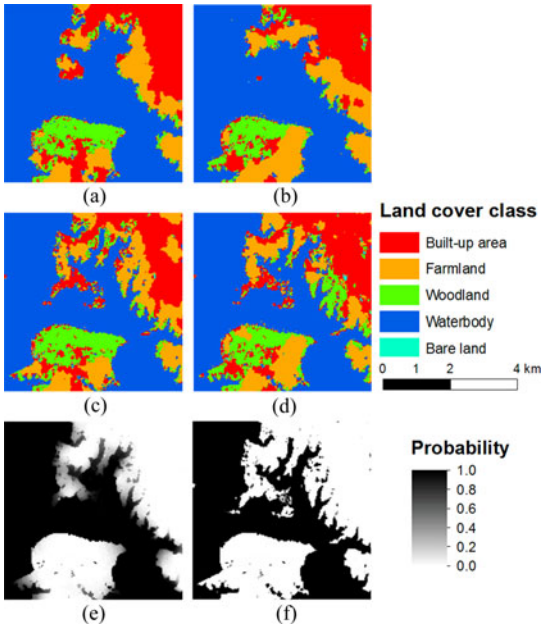

Fig. 16. Postclassification results of a portion of the Landsat 8 OLI image based on the NN preclassification and the sparse sample dataset for the Wuhan study area. (a) and (b) Two simulated realizations by coMCRF. (c) and (d) Two simulated realizations by SS-coMCRF. (e) and (f) The occurrence probability maps of waterbody produced by coMCRF and SS-coMCRF, respectively.

V. Conclusion

Two mutually complementary spatial similarity measures, the Jaccard index and the SCM, were combined as an integrated constraining factor and incorporated into the coMCRF model for land cover postclassification, in order to reduce the smoothing effect, particularly the loss of geometric features (e.g., shapes and boundaries) of land cover objects in postclassification maps.

The case studies demonstrated that the SS-coMCRF model reduced the smoothing effect of the existing coMCRF model and is effective in capturing more geometric shapes of land cover objects and preserving more details (e.g., tiny patches) in postclassification maps. Given the same expert-interpreted sample data, the land cover postclassifications by SS-coMCRF, and those by coMCRF both made apparent improvement in OA over the preclassifications by NN and SVM classifiers. Although SS-coMCRF did not show obvious advantages over coMCRF in OA improvement in land cover postclassifications, it did a much better job in capturing the geometric shapes of land cover objects, especially linear stripes and boundaries of land cover classes with distinct spectral reflectance values. This is exactly the goal we hoped to achieve by incorporating spectral similarity measures. The reason for the improvement in geometric features of land cover objects should be that SS-coMCRF utilized the spectral information more sufficiently (through incorporating pixel spectral similarity measures calculated from the spectral data of the original remotely sensed image) than coMCRF did. A visible tradeoff for SS-coMCRF is that it may keep some noise and tiny patches in postclassification maps, and the kept noise and tiny patches may not be correctly classified. In general, the SS-coMCRF model can be a promising method for land cover/use postclassification, especially when geometric shapes and linear features are emphasized.

References

[1] S. E. Franklin and M. A. Wulder, "Remote sensing methods in medium spatial resolution satellite data land cover classification of large areas," *Prog. Phys. Geogr.*, vol. 26, no. 2, pp. 173–205, 2002.
[2] T. Kavzoglu and I. Colkesen, "A kernel functions analysis for support vector machines for land cover classification," *Int. J. Appl. Earth Obs. Geoinf.*, vol. 11, no. 5, pp. 352–359, 2009.
[3] D. Lu and Q. Weng, "A survey of image classification methods and techniques for improving classification performance," *Int. J. Remote Sens.*, vol. 28, no. 5, pp. 823–870, 2007.
[4] D. M. Rogge, B. Rivard, J. Zhang, A. Sanchez, J. Harris, and J. Feng, "Integration of spatial–spectral information for the improved extraction of endmembers," *Remote Sens. Environ.*, vol. 110, no. 3, pp. 287–303, 2007.
[5] D. Lu, P. Mausel, M. Batistella, and E. Moran, "Comparison of land-cover classification methods in the Brazilian Amazon Basin," *Photogramm. Eng. Remote Sens.*, vol. 70, no. 6, pp. 723–731, 2004.
[6] J. Benediktsson, P. H. Swain, and O. K. Ersoy, "Neural network approaches versus statistical methods in classification of multisource remote sensing data," *IEEE Trans. Geosci. Remote Sens.*, vol. 28, no. 4, pp. 540–552, Jul. 1990.
[7] F. S. Erbek, C. Özkan, and M. Taberner, "Comparison of maximum likelihood classification method with supervised artificial neural network algorithms for land use activities," *Int. J. Remote Sens.*, vol. 25, no. 9, pp. 1733–1748, 2004.
[8] M. Brown, S. R. Gunn, and H. G. Lewis, "Support vector machines for optimal classification and spectral unmixing," *Ecol. Model.*, vol. 120, no. 2, pp. 167–179, 1999.
[9] C. W. Hsu and C. J. Lin, "A comparison of methods for multiclass support vector machines," *IEEE Trans. Neural Netw.*, vol. 13, no. 2, pp. 415–425, 2002.
[10] N. W. Park, K. H. Chi, and B. D. Kwon, "Geostatistical integration of spectral and spatial information for land-cover mapping using remote sensing data," *Geosci. J.*, vol. 7, no. 4, pp. 335–341, 2003.
[11] H. Buddenbaum, M. Schlerf, and J. Hill, "Classification of coniferous tree species and age classes using hyperspectral data and geostatistical methods," *Int. J. Remote Sens.*, vol. 26, no. 24, pp. 5453–5465, 2005.
[12] E. Binaghi, P. Madella, M. G. Montesano, and A. Rampini, "Fuzzy contextual classification of multisource remote sensing images," *IEEE Trans. Geosci. Remote Sens.*, vol. 35, no. 2, pp. 326–340, Mar. 1997.
[13] Q. Jackson and D. Landgrebe, "Adaptive Bayesian contextual classification based on Markov random fields," *IEEE Trans. Geosci. Remote Sens.*, vol. 40, no. 11, pp. 2454–2463, Nov. 2002.
[14] M. C. Dobson, L. E. Pierce, and F. T. Ulaby, "Knowledge-based land-cover classification using ERS-1/JERS-1 SAR composites," *IEEE Trans. Geosci. Remote Sens.*, vol. 34, no. 1, pp. 83–99, Jan. 1996.
[15] A. E. Daniels, "Incorporating domain knowledge and spatial relationships into land cover classifications: A rule-based approach," *Int. J. Remote Sens.*, vol. 27, no. 14, pp. 2949–2975, 2006.
[16] Z. Wu, Q. Wang, A. Plaza, J. Li, L. Sun, and Z. Wei, "Parallel spatial–spectral hyperspectral image classification with sparse representation and Markov random fields on GPUs," *IEEE J. Sel. Topics Appl. Earth Obs. Remote Sens.*, vol. 8, no. 6, pp. 2926–2938, Jun. 2015.
[17] S. M. de Jong, T. Hornstra, and H. G. Maas, "An integrated spatial and spectral approach to the classification of Mediterranean land cover types: The SSC method," *Int. J. Appl. Earth Obs. Geoinf.*, vol. 3, no. 2, pp. 176–183, 2001.
[18] O. Debeir, I. Van den Steen, P. Latinne, P. Van Ham, and E. Wolff, "Textural and contextual land-cover classification using single and multiple classifier systems," *Photogramm. Eng. Remote Sens.*, vol. 68, no. 6, pp. 597–606, 2002.
[19] X. Li, Q. Meng, X. Gu, T. Jancso, T. Yu, K. Wang, and S. Mavromatis, "A hybrid method combining pixel-based and object-oriented methods and its application in Hungary using Chinese HJ-1 satellite images," *Int. J. Remote Sens.*, vol. 34, no. 13, pp. 4655–4668, 2013.
[20] J. R. Jensen, *Introductory Digital Image Processing: A Remote Sensing Perspective*, 3rd ed. London, U.K.: Pearson College Division, 2005.
[21] V. Mesev, "The use of census data in urban image classification," *Photogramm. Eng. Remote Sens.*, vol. 64, no. 5, pp. 431–436, 1998.
[22] H. Huang, J. J. Legarsky, S. Gudimetla, and C. H. Davis, "Post-classification smoothing of digital classification map of St. Louis, Missouri," presented at the IEEE Int. Geosci. Remote Sens. Symp., Anchorage, AK, USA, Sep. 20–24, 2004.

[23] Y. Qian, F. Qiu, J. Chang, and K. Zhang, "Visualization-informed noise elimination and its application in processing high-spatial-resolution remote sensing imagery," *Comput. Geosci.*, vol. 34, no. 1, pp. 35–52, 2008.
[24] L. Zheng, L. Wan, H. Huo, and T. Fang, "A noise removal approach for object-based classification of VHR imagery via post-classification," in *Proc. IEEE Int. Conf. Audio, Lang. Image Process.*, 2014, pp. 915–920.
[25] R. Manandhar, I. O. A. Odeh, and T. Ancev, "Improving the accuracy of land use and land cover classification of Landsat data using post-classification enhancement," *Remote Sens.*, vol. 1, no. 3, pp. 330–344, 2009.
[26] Y. Zhang, "Optimisation of building detection in satellite images by combining multispectral classification and texture filtering," *ISPRS J. Photogramm. Remote Sens.*, vol. 54, no. 1, pp. 50–60, 1999.
[27] A. Puissant, J. Hirsch, and C. Weber, "The utility of texture analysis to improve per-pixel classification for high to very high spatial resolution imagery," *Int. J. Remote Sens.*, vol. 26, no. 4, pp. 733–745, 2005.
[28] W. L. Stefanov, M. S. Ramsey, and P. R. Christensen, "Monitoring urban land cover change: An expert system approach to land cover classification of semiarid to arid urban centers," *Remote Sens. Environ.*, vol. 77, no. 2, pp. 173–185, 2001.
[29] O. Kahya, B. Bayram, and S. Reis, "Land cover classification with an expert system approach using Landsat ETM imagery: A case study of Trabzon," *Environ. Monit. Assess.*, vol. 160, nos. 1–4, pp. 431–438, 2010.
[30] W. R. Tobler, "A computer movie simulating urban growth in the Detroit region," *Econ. Geogr.*, vol. 46, pp. 234–240, 1970.
[31] J. Carvalho, A. Soares, and A. Bio, "Improving satellite images classification using remote and ground data integration by means of stochastic simulation," *Int. J. Remote Sens.*, vol. 27, no. 16, pp. 3375–3386, 2006.
[32] W. Li, C. Zhang, M. R. Willig, D. K. Dey, G. Wang, and L. You, "Bayesian Markov chain random field cosimulation for improving land cover classification accuracy," *Math. Geosci.*, vol. 47, no. 2, pp. 123–148, 2014.
[33] W. Zhang, W. Li, and C. Zhang, "Land cover post-classifications by Markov chain geostatistical cosimulation based on pre-classifications by different conventional classifiers," *Int. J. Remote Sens.*, vol. 37, no. 4, pp. 926–949, 2016.
[34] Y. Tang, P. M. Atkinson, N. A. Wardrop, and J. Zhang, "Multiple-point geostatistical simulation for post-processing a remotely sensed land cover classification," *Spatial Stat.*, vol. 5, pp. 69–84, 2013.
[35] S. Homayouni and M. Roux, "Hyperspectral image analysis for material mapping using spectral matching," presented at the Int. Soc. Photogramm. Remote Sens. Congr., Istanbul, Turkey, 2004.
[36] R. R. Nidamanuri and B. Zbell, "Normalized spectral similarity score (NS^3) as an efficient spectral library searching method for hyperspectral image classification," *IEEE J. Sel. Topics Appl. Earth Obs. Remote Sens.*, vol. 4, no. 1, pp. 226–240, Mar. 2011.
[37] M. Naresh Kumar *et al.*, "A new hybrid spectral similarity measure for discrimination among Vigna species." *Int. J. Remote Sens.*, vol. 32, no. 14, pp. 4041–4053, 2011.
[38] M. Pal and P. M. Mather, "An assessment of the effectiveness of decision tree methods for land cover classification," *Remote Sens. Environ.*, vol. 86, no. 4, pp. 554–565, 2003.
[39] C. S. Murthy, P. V. Raju, and K. V. S. Badrinath, "Classification of wheat crop with multi-temporal images: performance of maximum likelihood and artificial neural networks," *Int. J. Remote Sens.*, vol. 24, no. 23, pp. 4871–4890, 2003.
[40] T. Kavzoglu and P. M. Mather, "The use of backpropagating artificial neural networks in land cover classification," *Int. J. Remote Sens.*, vol. 24, no. 23, pp. 4907–4938, 2003.
[41] M. Pal and P. M. Mather, "Assessment of the effectiveness of support vector machines for hyperspectral data," *Future Gener. Comput. Syst.*, vol. 20, no. 7, pp. 1215–1225, 2004.
[42] G. M. Foody and A. Mathur, "A relative evaluation of multiclass image classification by support vector machines," *IEEE Trans. Geosci. Remote Sens.*, vol. 42, no. 6, pp. 1335–1343, Jun. 2004.
[43] W. Li, "Markov chain random fields for estimation of categorical variables," *Math. Geol.*, vol. 39, no. 3, pp. 321–335, 2007.
[44] W. Li, C. Zhang, D. K. Dey, and M. R. Willig, "Updating categorical soil maps using limited survey data by Bayesian Markov chain cosimulation," *Sci. World J.*, vol. 2013, 2013, Art. no. 587284.
[45] W. Li, "Transiograms for characterizing spatial variability of soil classes," *Soil Sci. Soc. Amer. J.*, vol. 71, no. 3, pp. 881–893, 2007.
[46] C. Zheng and L. Wang, "Semantic segmentation of remote sensing imagery using object-based Markov random field model with regional penalties," *IEEE J. Sel. Topics Appl. Earth Obs. Remote Sens.*, vol. 8, no. 5, pp. 1924–1935, May 2015.
[47] W. Li and C. Zhang, "A random-path Markov chain algorithm for simulating categorical soil variables from random point samples," *Soil Sci. Soc. Amer. J.*, vol. 71, no. 3, pp. 656–668, 2007.
[48] F. van der Meer, "The effectiveness of spectral similarity measures for the analysis of hyperspectral imagery," *Int. J. Appl. Earth Obs. Geoinf.*, vol. 8, no. 1, pp. 3–17, 2006.
[49] P. Jaccard, "Distribution de la Flore Alpine: Dans le Bassin des dranses et dans quelques régions voisines," *Bull. Soc. Vaud. Sci. Nat.*, vol. 37, pp. 241–272, 1901.
[50] S. Niwattanakul, J. Singthongchai, E. Naenudorn, and S. Wanapu, "Using of Jaccard coefficient for keywords similarity," in *Proc. Int. Multi Conf. Eng. Comput. Scientists*, 2013, vol. 1, pp. 13–15.
[51] J. N. Sweet, "The spectral similarity scale and its application to the classification of hyperspectral remote sensing data," in *Proc. IEEE Workshop Adv. Techn. Anal. Remotely Sensed Data*, Washington DC, USA, Oct. 27–28, 2003, pp. 92–99.
[52] U.S. Geological Survey. Frequently asked questions about the Landsat missions. (2016). [Online]. Available: http://landsat.usgs.gov//tools_faq.php
[53] W. Li and C. Zhang, "Linear interpolation and joint model fitting of experimental transiograms for Markov chain simulation of categorical spatial variables," *Int. J. Geogr. Inf. Sci.*, vol. 24, no. 6, pp. 821–839, 2010.

Weixing Zhang received the B.E. degree from China University of Geosciences, Wuhan, China, in 2012, the M.A. degree from the University of Connecticut, Storrs, CT, USA, in 2015, where he is currently working toward the Ph.D. degree in the Department of Geography.

His current research interests include land cover/use classification, cloud computing in image processing, and web-based GIS applications.

Weidong Li received the Ph.D. degree in soil science from China Agricultural University, Beijing, China, in 1995.

He is currently a Research Professor in the Department of Geography, University of Connecticut, Storrs, CT, USA. His current research interests include spatial statistics, GIScience, and resource and environment informatics.

Chuanrong Zhang received the Ph.D. degree in geography from the University of Wisconsin, Milwaukee, WI, USA, in 2004.

She is currently a Professor in the Department of Geography and Center of Environmental Sciences and Engineering, University of Connecticut, Storrs, CT, USA. Her current research interests include GIScience, spatial modeling, remote sensing, and landscape ecology for environment and resource management.

Xiaojiang Li received the M.S. degree from the Institute of Remote Sensing and Digital Earth, Chinese Academy of Science, Beijing, China, in 2013. He is currently working toward the Ph.D. degree in the Department of Geography, University of Connecticut, Storrs, CT, USA.

His current research interests include urban environment modeling, remote sensing, and GIScience.